Ultrasonics 106 (2020) 106160

Contents lists available at ScienceDirect

Ultrasonics

journal homepage: www.elsevier.com/locate/ultras

The complexity of surface acoustic wave fields used for microfluidic applications

R. Weser[a,*], A. Winkler[a], M. Weihnacht[b], S. Menzel[a], H. Schmidt[a]

[a] Leibniz Institute for Solid State and Materials Research Dresden, SAWLab Saxony, Helmholtzstr. 20, 01069 Dresden, Germany
[b] InnoXacs GmbH, Am Muehlfeld 34, 01744 Dippoldiswalde, Germany

ARTICLE INFO

Keywords:
Surface acoustic wave (SAW)
SAW actuator
Microfluidics
Wave field
Standing SAW
Acoustic tweezers

ABSTRACT

Using surface acoustic waves (SAW) for the agitation and manipulation of fluids and immersed particles or cells in lab-on-a-chip systems has been state of the art for several years. Basic tasks comprise fluid mixing, atomization of liquids as well as sorting and separation (or trapping) of particles and cells, e.g. in so-called acoustic tweezers. Even though the fundamental principles governing SAW excitation and propagation on anisotropic, piezoelectric substrates are well-investigated, the complexity of wave field effects including SAW diffraction, refraction and interference cannot be comprehensively simulated at this point of time with sufficient accuracy. However, the design of microfluidic actuators relies on a profound knowledge of SAW propagation, including superposition of multiple SAWs, to achieve the predestined functionality of the devices. Here, we present extensive experimental results of high-resolution analysis of the lateral distribution of the complex displacement amplitude, i.e. the wave field, alongside with the electrical *S*-parameters of the generating transducers. These measurements were carried out and are compared in setups utilizing travelling SAW (tSAW) excited by single interdigital transducer (IDT), standing SAW generated between two IDTs (1DsSAW, 1D acoustic tweezers) and between two pairs of IDTs (2DsSAW, 2D acoustic tweezers) with different angular alignment in respect to pure Rayleigh mode propagation directions and other practically relevant orientations. For these basic configurations, typically used to drive SAW-based microfluidics, the influence of common SAW phenomena including beam steering, coupling coefficient dispersion and diffraction on the resultant wave field is investigated. The results show how tailoring of the acoustic conditions, based on profound knowledge of the physical effects, can be achieved to finally realize a desired behavior of a SAW-based microacoustic-fluidic system.

1. Introduction

Active microfluidic devices using surface acoustic waves (SAW) have been demonstrated for several tasks including fluid mixing, atomization and manipulation of immersed particles and cells [1–4]. Thereby, the knowledge of the SAW wave field (i.e. the lateral distribution of displacement amplitude) is mandatory since it determines all subsequent acoustofluidic effects. Rayleigh type SAWs are usually used for actuation purposes since this wave mode is characterized by a comparatively large surface normal component of displacement which mainly provokes the transfer of momentum to the bulk acoustic wave (BAW) in the fluid [5]. Almost all SAW-driven microfluidic devices typically use Rayleigh type SAWs on 128° rotated Y-cut lithium niobate (128°Y $LiNbO_3$) substrates [6–9]. Besides travelling SAW (tSAW) excited by a single IDT oriented at a certain angle with respect to the X-direction of the crystal, more complex wave fields arising from the superposition of at least two tSAWs are often used, i.e. for acoustic tweezer setups. Particle sorting within a microchannel is usually achieved using two counter-propagating tSAWs excited to generate a standing SAW in one dimension (1DsSAW) [10–15]. The same setup also can be used for SAW-based atomization of fluids [16,17]. The superposition of two 1DsSAWs with different propagation directions allows for the generation of a two-dimensional standing SAW (2DsSAW), showing high relevance for microparticle manipulation and trapping in 2D SAW-based acoustic tweezers [18–22]. Fig. 1 exemplarily shows the measured SAW wave field for a setup with four IDTs typically used for acoustic tweezers. A comparable IDT setup also was used in a recent publication demonstrating the acoustic tweezers capability [23]. For such kinds of complex wave fields (2DsSAW), possessing at least one standing wave with orientation different from the X-axis, effects including beam steering, different coupling coefficients and phase velocities as well as the appearance of other SAW modes have to be taken

* Corresponding author.
E-mail address: r.weser@ifw-dresden.de (R. Weser).

https://doi.org/10.1016/j.ultras.2020.106160
Received 18 March 2019; Received in revised form 27 January 2020; Accepted 13 February 2020
Available online 14 April 2020

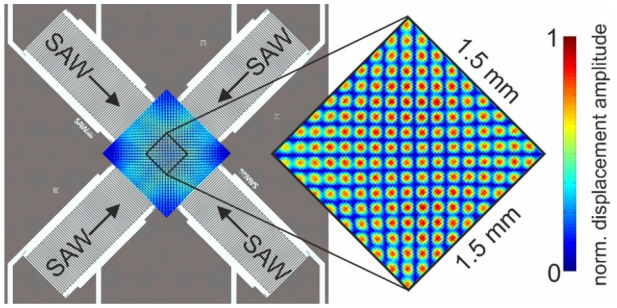

Fig. 1. Example of a complex SAW wave field with standing waves in two dimensions (2DsSAW) generated by a layout of four interdigital transducers (solid finger IDT with 150 µm periodicity) on 128°Y $LiNbO_3$, rotated by ± 45° with respect to X-direction of the crystal. All IDTs are excited with the same power at equal frequency (23.69 MHz). Lateral distribution of surface normal displacement, measured with laser Doppler vibrometer (Polytec UHF 120) at 23.69 MHz, and microscopic image are overlayed for illustration.

into account since the substrate material is anisotropic with orientation-dependent SAW properties [24]. While focusing on 128°Y $LiNbO_3$ as common substrate material for SAW-driven microfluidics, we essentially investigate the influence of the mentioned effects on the SAW wave field peculiarity and discuss consequences for microfluidic applications.

2. SAW propagation fundamentals on anisotropic substrates

2.1. Travelling SAW (tSAW) propagation

The most common way to excite a surface acoustic wave is to utilize an interdigital transducer (IDT) deposited on a piezoelectric substrate. The SAW is excited by applying an alternating electrical voltage to the pair of comb-shaped IDT electrodes giving rise to local vibrations that superimpose to a surface acoustic wave propagating along the substrate surface. Considering a plane wave with angular frequency $\omega = 2\pi \cdot f$ and wave vector $\boldsymbol{k}$, the propagation of SAW in a half-infinite medium (halfspace) can be described in terms of displacement $\boldsymbol{u}$

$$\boldsymbol{u} = \hat{\boldsymbol{u}} \cdot \exp[j(\omega t - \boldsymbol{k} \cdot \boldsymbol{x})]$$

and electric potential ϕ

$$\phi = \hat{\phi} \cdot \exp[j(\omega t - \boldsymbol{k} \cdot \boldsymbol{x})]$$

based on propagation vector $\boldsymbol{x} = (x_1, x_2, x_3)$ with directions x_1 along propagation direction and x_2 perpendicular to x_1, both parallel to the substrate surface, as well as with x_3 in surface normal direction.

Most often, single crystalline, anisotropic materials are used as substrate. Hence, the crystal cut orientation as well as the propagation angle θ are closely connected to important parameters of SAW excitation and propagation. The phase velocity and polarization of the SAW as well as the coupling coefficient and beam steering are of particular interest, especially for the superposition of SAWs. In this work, we focus on Rayleigh type SAWs excited on the common 128°Y $LiNbO_3$ (128° rotated Y-cut lithium niobate), as they are typically used for fluid actuation purposes due to the dominating component of surface normal displacement and a neglectable horizontal shear component – in case of propagation along X-axis: $|u_3|/|\boldsymbol{u}| = 0.75$ and $|u_2|/|\boldsymbol{u}| = 0.04$ [25].

128°Y $LiNbO_3$ has a strong piezoelectric coupling yielding large displacement amplitudes. Piezoelectric coupling is specified by the SAW coupling coefficient [24]:

$$K^2 = 2\frac{v_f - v_m}{v_f}$$

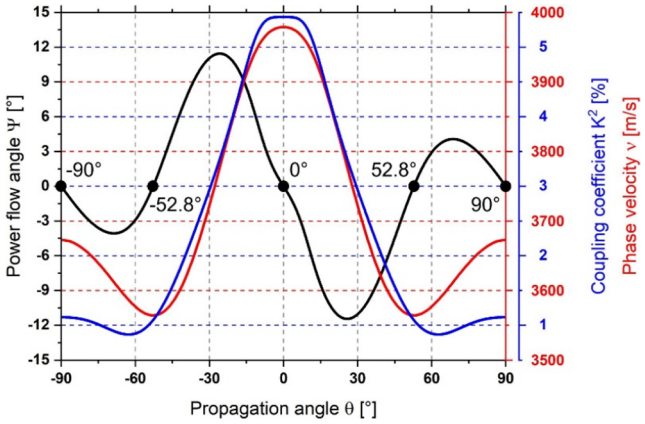

Fig. 2. Orientation dependent properties of Rayleigh waves propagating on 128°Y $LiNbO_3$ (propagation angle with respect to X-axis).

Here, v_f and v_m are the SAW phase velocities, calculated for free and electrically short-circuited surface, respectively. 128°Y $LiNbO_3$ has a maximum coupling coefficient $K^2 = 5.4\%$ for propagation along X-axis (Fig. 2, $\theta = 0^\circ$). For an anisotropic substrate, the propagation velocity of a single plane wave (i.e. their phase velocity v) is a function of propagation direction $v(\theta)$ (Fig. 2). This also causes an orientation dependent coupling coefficient $K^2(\theta)$ as well as beam steering can occur since the energy of a SAW of finite width forming a SAW beam propagates along the beam direction rather than in the propagation direction x_1 given by the wave vector $\boldsymbol{k}$ (Fig. 3b). The beam direction is equal to the direction of group velocity which is defined to be normal to the angular wave vector dispersion resulting from the so-called slowness curve:

$$k(\theta) = \omega / v(\theta)$$

Anisotropic materials are characterized by a slowness curve deviating from the circular shape (Fig. 3a) provoking the beam direction to be generally no longer parallel to the propagation direction. The angle between the SAW wave vector (defining the propagation direction) and the beam direction (given by the power flow) is often called power flow angle ψ:

$$\tan\psi = \frac{1}{v}\frac{dv}{d\theta}$$

A geometric illustration of the tangent function can be seen in Fig. 3. Usually the power flow angle is small, so that $\tan\psi \approx \psi$.

Besides angular dispersion of SAW phase velocity, Fig. 2 shows the angle dependent behavior of the coupling coefficient and of the power flow angle for 128°Y $LiNbO_3$. Calculations are based on material constants given in [26]. The coupling coefficient is axially symmetric with respect to the rotation angle with a maximum at $\theta = 0^\circ$. The power flow angle is centrally symmetric showing zero crossings at $\theta = 0^\circ; \pm 52.8^\circ; \pm 90^\circ$ (marked in Fig. 2). Thus, the power flow is equal to the wave propagation direction (i.e. the wave vector) only for these specific propagation angles, otherwise significant beam steering ($\psi \neq 0$) occurs.

2.2. Superposition of multiple SAWs

So far, a single surface acoustic wave propagating along an anisotropic substrate has been considered. In this case, the corresponding wave field (lateral distribution of surface displacement) is characterized by the existence of a travelling wave based on the assumption of a laterally infinite substrate and negligible reflections from the edges. For many applications, however, more complex wave fields are required. In

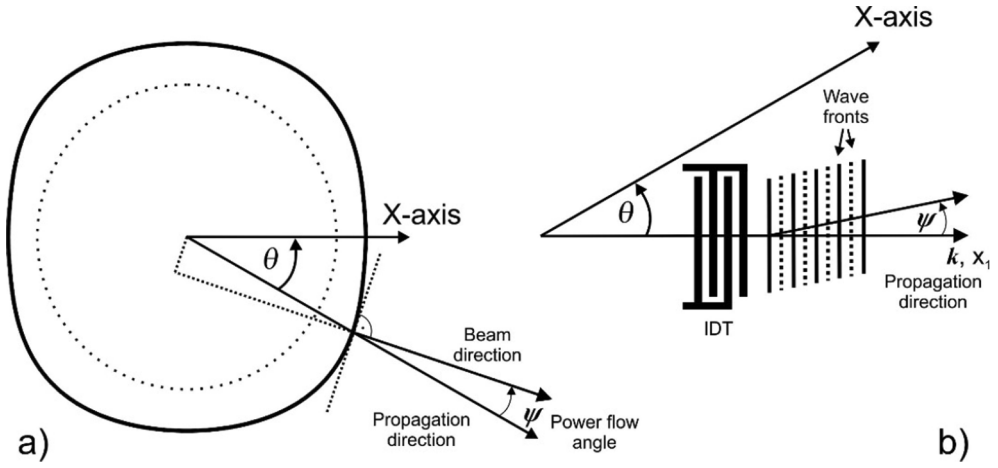

Fig. 3. Geometric interpretation of the beam steering effect due to the orientation dependent SAW velocity $v(\theta)$ on anisotropic substrate materials: (a) qualtitative slowness curve for 128°Y $LiNbO_3$ w.r.t. to X-axis (dashed circle line is given for comparison purposes), beam direction (normal to the slowness curve) and power flow angle ψ, (b) SAW beam propagating in front of the IDT with wave fronts perpendicular to the propagation direction x_1 and power flow angle $\psi \neq 0$.

particular, standing waves are essential for microfluidic actuators as sorting or trapping of fluid immersed particles or cells necessitates the presence of bulk acoustic wave (BAW) nodes inside the fluid vessel. These BAW nodes can arise from wave reflection at boundaries (e.g. between fluid and vessel walls) and subsequent wave interference [27,28], however are mostly provoked by standing SAW. Hence, the knowledge of SAW superposition is essential for designing tailored SAW fields to get a defined and controllable BAW field that generates the necessary forces inside the fluid.

Considering an acoustic wave propagating along the surface defined by lateral coordinates x and y and surface normal coordinate z, the time-dependent surface displacement $\boldsymbol{u} = (u_x, u_y, u_z)$ at position (x, y) can be specified by a localized harmonic oscillation:

$$\boldsymbol{u}(x, y, t) = \hat{\boldsymbol{u}}(x, y)\cdot\cos[\omega t + \boldsymbol{\varphi}(x, y)]$$

where $\hat{\boldsymbol{u}} = (\hat{u}_x, \hat{u}_y, \hat{u}_z)$ denotes the maximum amplitude and $\boldsymbol{\varphi} = (\varphi_x, \varphi_y, \varphi_z)$ the phase shift between specific positions related e.g. to the phase of the excitation signal. Every wave passing this position, contributes to the local displacement described by linear superposition:

$$\boldsymbol{u}(x, y, t) = \sum_i u_i(x, y, t) = \sum_i \hat{u}_i(x, y)\cdot\cos[\omega_i t + \varphi_i(x, y)]$$

assuming that nonlinear effects can be neglected. Nonlinearity may arise from higher order piezoelectric coupling effects or very large amplitudes.

The most commonly used application of SAW superposition (for actuation purposes) is realized by two counter-propagating SAWs. A pure standing wave only occurs if both waves exhibit parallel and plane wave fronts as well as they hold the same frequency ($\omega_1 = \omega_2$) and equal amplitude ($\hat{u}_1 = \hat{u}_2$). In this case, wave nodes are stationary (appear at fixed positions), do not vary with time and exhibit vanishing amplitude. If both waves possess different frequencies ($\omega_1 \neq \omega_2$), the wave nodes are not stationary in time, anymore. An additional modulation given by

$$\cos(\omega_1 t) + \cos(\omega_2 t) = 2\cos\left(\frac{\omega_1 + \omega_2}{2}t\right)\cos\left(\frac{\omega_1 - \omega_2}{2}t\right)$$

occurs, that contributes to the overall amplitude yielding a periodically rising and falling amplitude envelope. This so called beating (or surging) amplitude is characterized by the frequency $\omega_{beat} = |\omega_1 - \omega_2|$ and a corresponding period $T_{beat} = 2\pi/\omega_{beat}$.

3. Experiments

Experimental investigations on SAW propagation and superposition were carried out for three different IDT arrangements on 128°Y $LiNbO_3$. Each arrangement comprises two pairs of equal IDTs (λ/4-IDT, periodicity λ= 150 µm, aperture w= 2 mm, number of finger pairs N= 33, 3.5 mm distance between IDTs) oriented at different angles θ with respect to the X-direction (Fig. 4, Table 1). All three IDT setups according to Fig. 4 were fabricated via electron-beam evaporation and lift-off technique of subsequent layers of titanium (5 nm) and aluminum (295 nm). The electrical impedance of IDT was matched to 50 Ω for X-propagation direction ($X + 0^{\circ}$) using a proprietary software based on the coupling-of-modes (COM) theory [24]. The electrical mismatch for other propagation directions can be partially counter-balanced by an additional (external) impedance matching [29]. Additionally, the whole SAW chip was coated with a sputter-deposited SiO_2 layer of 1 µm thickness as corrosion protection [30].

The SAW chips were mounted on a custom chip holder and electrically connected using printed circuit boards (PCB) comprising strip lines matched to 50 Ω characteristic impedance and gold-plated spring pins (Fig. 5). Highly viscous photoresist was applied to the surrounding of the IDTs as damping material in order to minimize the influence of acoustic reflections from substrate edges. If SAW reflections from the substrate edges are not sufficiently suppressed, they will contribute to the intended SAW field in between the IDTs. Thus, the size of the substrate will affect the SAW field because the time-of-flight of reflections is proportional to the dimensions of the substrate and will affect the phase of both, reflected SAW and superimposed SAW field. The thickness of the substrate should be chosen to be at least 1.5 times the SAW wavelength, in order to avoid flexural plate wave excitation. Characterization of the electrical behavior was carried out via electrical S-parameter measurements with a vector network analyzer (VNA, Agilent E5071C). The lateral distribution of surface normal displacement in terms of amplitude $\hat{u}_z(x, y)$ and phase $\varphi_z(x, y)$ was measured with a scanning laser Doppler vibrometer (LDV, Polytec UHF 120). A microscope objective with magnification of 20x (Mitutoyo) was used to form a laser spot of < 2.5 µm in diameter, which is small compared to the wavelength of the SAW (150 µm). The scan resolution was set to 15 µm in both lateral directions in order to ensure a sufficiently high number of measurement points per wavelength or half the wavelength in case of standing wave. This is a reasonable compromise between

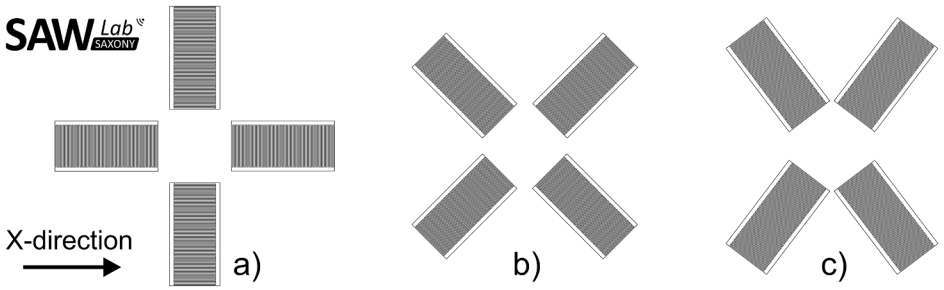

Fig. 4. Arrangements of interdigital transducers (IDTs) to investigate SAW superposition. IDTs exhibit different orientations w.r.t. X-direction: (a) $X + 0^{\circ}$ and $X + 90^{\circ}$ respectively, (b) $X \pm 45^{\circ}$ and (c) $X \pm 52.8^{\circ}$. Distance between two opposing IDTs is 3.5 mm.

desired resolution and the total number of measurement points (up to 52,000 points corresponding to a measurement time of 70 h) since the area of interest is quite large (12.25 mm^2) given by the distance of two opposing IDT [31].

All measurements were carried out at room temperature: (a) one single IDT rotated by $\theta = 0^{\circ}; 45^{\circ}; 52.8^{\circ}; 90^{\circ}$ with respect to X-direction was characterized. Therefore, the opposing IDT was mechanically damped (covered with photoresist) in order to suppress reflections and to achieve a pure travelling SAW (tSAW), (b) the superposition of two tSAWs excited by two opposing IDTs (rotated by $\theta = 0^{\circ}; \pm 45^{\circ}; \pm 52.8^{\circ}; 90^{\circ}$) was investigated. This kind of superposition is considered as a standing wave field within one lateral dimension (1DsSAW), (c) two 1DsSAWs superimposing at different propagation directions (Fig. 4, Table 1) were combined leading to a standing wave field in two lateral dimensions (2DsSAW).

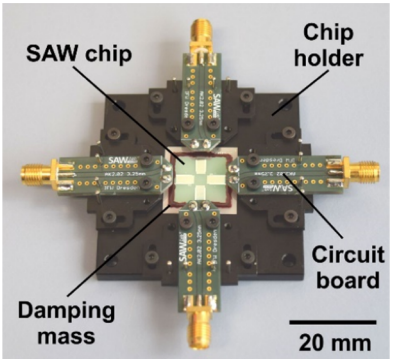

Fig. 5. SAW chip mounted on custom chip holder for mechanical retaining and electrical connection during experiments. Damping mass (highly viscous photoresist) is applied to suppress undesired SAW reflections at chip edges.

4. Results and discussion

4.1. Travelling SAW (tSAW)

The electrical characterization of a single IDT provides fundamental information on the excitation of SAW for different orientations with respect to X-direction (Fig. 6). The frequency dependent input reflection coefficient $|S_{11}|$ shows resonant behavior due the periodicity of IDT electrodes and the wavelength-to-frequency relationship $v = \lambda \cdot f$. The SAW wavelength λ is defined by the IDT electrode periodicity whereas the phase velocity v is given by the substrate material and the propagation orientation. Hence, a characteristic resonance peak occurs at which $|S_{11}|$ shows a minimum. In the present case, the related resonance frequencies are $f_{52.8^{\circ}} < f_{45^{\circ}} < f_{90^{\circ}} < f_{0^{\circ}}$ according to the different phase velocities (Fig. 2, Table 2). The lower the minimum value of electrical reflection ($|S_{11}|_{min}$), the less electric energy is reflected from the IDT towards the signal generator. If the characteristic impedances of IDT (Z_{IDT}) and generator (Z_0) are equal ($Z_{IDT} = Z_0$, typically Z_0= 50 Ω real), reflection completely vanishes ($|S_{11}| = 0$). In principle, the real part of admittance (conductance G) needs to be evaluated since it provides a more direct indicator for the amount of electric energy that is converted by the IDT into acoustic energy. Frequency dependence of $|S_{11}|$ and G

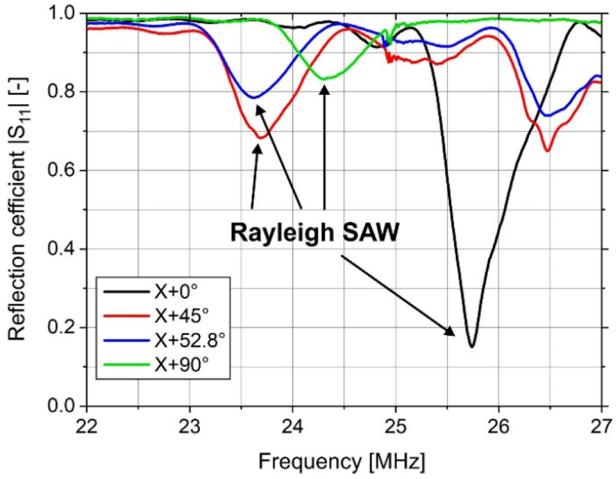

Fig. 6. Electrical characterization in terms of reflection coefficient $|S_{11}|$ of single interdigital transducers oriented at different angles w.r.t. X-direction on 128°Y $LiNbO_3$.

Table 1
Comparison of SAW propagation properties for the three IDT arrangements in Fig. 4.

Orientation of IDT pairs (two opposing IDTs) w.r.t. X-direction	$X + 0^{\circ}$ $X + 90^{\circ}$	$X \pm 45^{\circ}$	$X \pm 52.8^{\circ}$
Phase velocity	v=3979 m/s ($X + 0^{\circ}$) v=3672 m/s ($X + 90^{\circ}$)	v=3583 m/s	v=3564 m/s
Coupling coefficient	K^2=5.4% ($X + 0^{\circ}$) K^2=1.12% ($X + 90^{\circ}$)	K^2=1.56%	K^2=1.07%
Power flow angle	$\psi = 0^{\circ}$	$\psi = \mp 4.48^{\circ}$	$\psi = 0^{\circ}$
Orthogonality between both IDT pairs	yes	yes	no

Table 2
Electrical characteristics of IDTs with different orientation and comparison of resonance frequencies between theory and experiment. An IDT period (wavelength λ) of 150 µm and phase velocity v_0 of uncoated $LiNbO_3$ (Fig. 2) are considered for calculations of theoretical resonance frequencies f_0. Experimental resonance frequencies f_{exp} are obtained from electrical measurements (minimum of reflection coefficient $|S_{11}|_{min}$).

θ [°]	v_0 [m/s]	f_0 [MHz]	f_{exp} [MHz]	$\|S_{11}\|_{min}$	$(\|S_{11}\|_{min})^2$
0	3979	26.53	25.74	0.15	0.023
45	3583	23.89	23.69	0.68	0.462
52.8	3564	23.76	23.64	0.78	0.608
90	3672	24.48	24.32	0.83	0.689

show similar behavior for the presented IDT arrangements and thus, profound discussion can be based also on the reflection coefficient only.

If the SAW propagates along the X-direction ($X + 0^\circ$, Fig. 6, black line), the electric reflection coefficient shows the lowest minimum $|S_{11}|_{min}$ of all arrangements. This also corresponds to the lowest power reflection of $(|S_{11}|_{min})^2$, however, a non-ideal impedance matching can be obtained since the impedance of the IDT is $Z(25.74\ \text{MHz}) = (65.4\text{-}j*8.08)\ \Omega \neq 50\ \Omega$. Nevertheless, the $|S_{11}|_{min}$ for $\theta = 0^\circ$ is markedly lower compared to the cases $\theta \neq 0^\circ$. Thus, more electric energy is reflected and no longer available for SAW excitation. Higher $|S_{11}|_{min}$ is caused by a rather large impedance mismatch since the IDT design is optimized for X-direction. IDT arrangements at $X + 45^\circ$ and $X + 52.8^\circ$ show two significant resonance frequencies at $f \approx 23.7$ MHz and $f \approx 26.5$ MHz. The resonance at $f_{exp} \approx 23.7$ MHz is related to Rayleigh-type SAW excitation, whereas other acoustic wave modes, e.g. bulk waves inside the substrate, are excited at higher frequencies (Fig. 8).

Values of frequency extracted from electrical measurements (f_{exp}) differ from those calculated (f_0) via the simple equation $f_0 = v_0/\lambda$ (Table 2). This difference is mainly caused by differing phase velocities since the phase velocity v_{IDT} within the IDT differs from that of uncoated $LiNbO_3$ due to presence of electrode metallization and the additional SiO_2 layer. Moreover, the resonance frequency f_{exp} is not equivalent to the synchronous frequency of the IDT $f_S = v_{IDT}/\lambda$ because internal reflections at the electrodes cause an asymmetry of resonance peaks of reflection coefficient $|S_{11}|$ and thus, a resonance frequency which is slightly lower in these cases than the synchronous frequency ($f_{exp} < f_S$).

The wave fields in front of single IDTs oriented at different angles θ with respect to the X-direction are shown in Fig. 7. In general, a travelling SAW (tSAW) exhibits a continuous phase shift with 360° (± 180°) periodicity (Fig. 7, right column). The amplitude of the complex displacement (Fig. 7, left column) shows a characteristic behavior for the different propagation directions. In case of $X + 0^\circ$ and $X + 90^\circ$ an almost ideal symmetry with respect to the beam axis ($y = 0$), i.e. perpendicular to the propagation direction, can be observed. The same is valid for $X + 52.8^\circ$ although the symmetry axis is slightly shifted ($y > 0$). However, for these three orientations no beam steering occurs and thus, the power flow is parallel to the SAW propagation direction. For $X + 45^\circ$ no symmetry is observed due to beam steering. A negative power flow angle can be observed ($\psi < 0$) since the rotation angle of IDT is positive ($\theta = +45^\circ$). In any case, the beam profiles indicate a slight focusing effect, i.e. the width of the SAW beam profile decreases with increasing distance from the IDT ($x > 0$). This is caused by diffraction effects due to the limited aperture of IDTs.

The maximum displacement amplitudes of tSAW arise at the same frequencies (f_{exp}) that can be determined from electrical measurements ($|S_{11}|_{min}$), regardless of the particular propagation direction. Even for $X + 45^\circ$ and $X + 52.8^\circ$ this relationship holds true although the electrical behavior indicates a second resonance at $f \approx 26.50$ MHz. Fig. 8 exemplarily compares amplitudes at $f_{exp} = 23.69$ MHz with those at $f = 26.50$ MHz for $X + 45^\circ$. Beside an obvious decrease of amplitude at $f = 26.50$ MHz, a distortion of the beam profile can be identified. This provides an indication of bulk waves excited in the substrate interfering with the surface waves. The influence of excitation frequency on the wave field evolution is exemplary shown in a supplemental video 1 for $X + 45^\circ$.

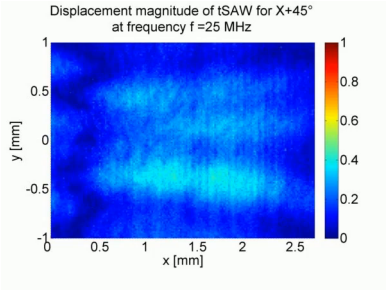

video 1.

Besides the previously discussed effects of wave field characteristics at resonance, the frequency at which the IDT is operated considerably affects the lateral distribution of displacement amplitude as expected. The amplitude decreases below and above resonance frequency since the excitation efficiency of the IDT decreases with increasing mismatch of transducer period, defined by the layout, and resultant SAW wavelength varying as a function of excitation frequency. Eventually, the angular spectrum of the excited SAW is altered by changing the driving frequency.

This leads to a lateral amplitude distribution which can significantly differ from the intended pattern obtained at resonance frequency due to emerging distinctive minima and maxima zones within the SAW beam. However, in case of $\theta = 0^\circ$ a relatively wide frequency range between 25.4 MHz and 26.4 MHz can be used for proper tSAW operation. The related wave fields exhibit substantially similar patterns (Fig. 9) and the reflection coefficient is $|S_{11}| < 0.8$ for the whole range (cf. Fig. 6) indicating an adequate acoustic excitation efficiency.

4.2. Standing SAW in one dimension (1DsSAW)

Fig. 10 shows the electrical reflection and transmission of an IDT pair with 3.5 mm distance for each of the four propagation angles. In principle, a similar electrical behavior compared to single IDTs (cf. Fig. 6) can be found: for $\theta = 0^\circ$ transmission is considerably higher compared to $\theta \neq 0^\circ$, which again is caused by impedance mismatch of the rotated setups. However, the presence of an opposing IDT causes additional reflections leading to additional minima and maxima in the $|S_{11}|$ curve. SAW reflection at the opposing IDT can be clearly identified using time domain representation of $|S_{11}|$ obtained by Fourier transform. Exemplary for SAW propagation along X-axis, $|S_{11}|$ time domain curves for single IDT and IDT pair are shown in Fig. 10b. They are equal for a travel time $t < 2$ µs since there is no influence of reflections from the opposing IDT, whereas for $t > 2$ µs the $|S_{11}|$ of the IDT pair shows significant peaks around $t \approx 3.5$ µs and $t \approx 7$ µs. Both can be assigned to two and four times the distance between both IDTs (2 × 7 mm and 4 × 7 mm), respectively. Hence, SAW reflections from the opposing IDT evoke changes of electrical behavior also in the frequency domain. The superposition of two counter-propagating tSAWs of the same frequency yields a standing SAW pattern in one lateral direction (1DsSAW). At positions where both tSAWs have equal amplitudes, a pure standing wave field without travelling portions exists, while at other positions combined standing/travelling pattern or localized pure

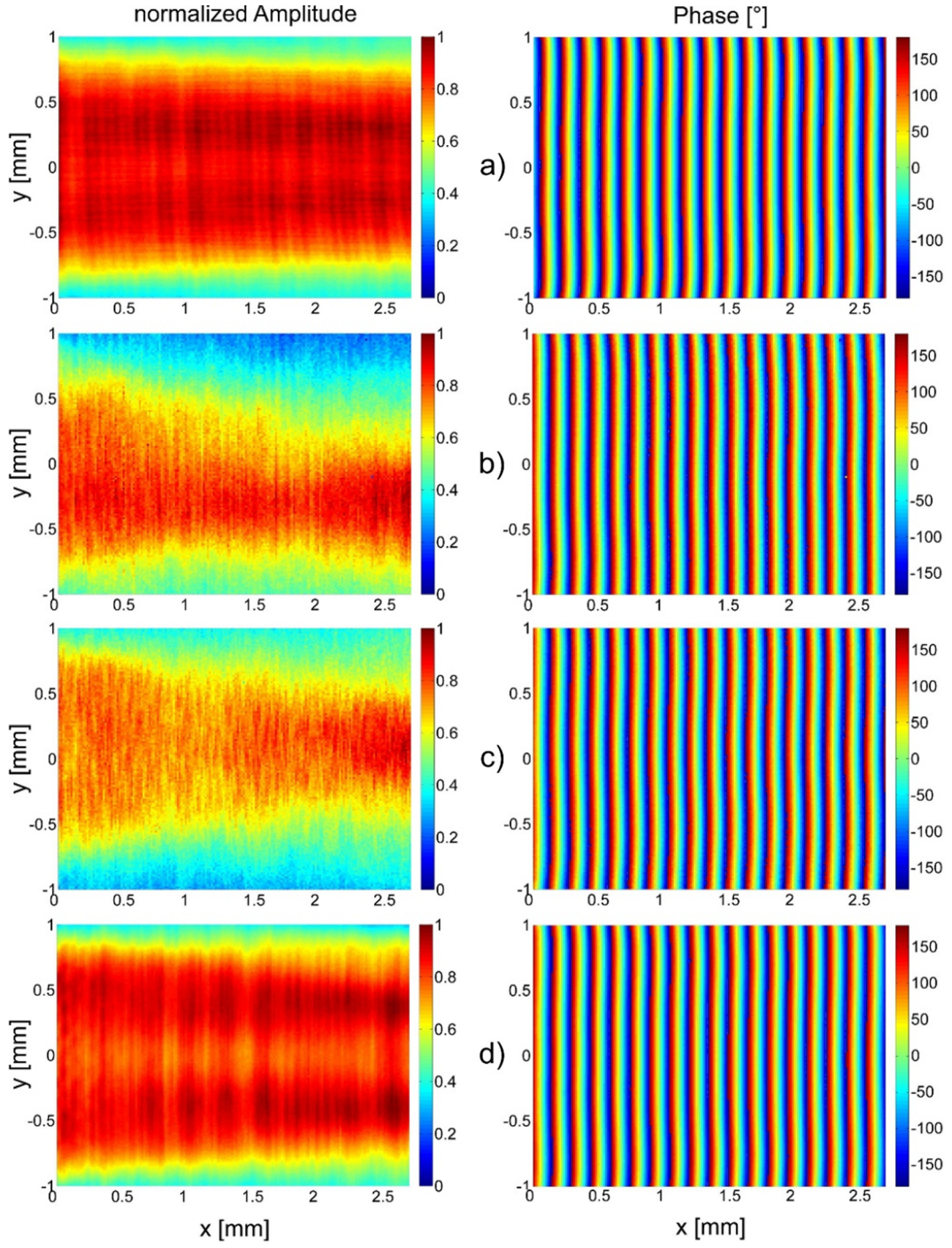

Fig. 7. Wave fields in front of single IDTs oriented at different angles w.r.t. to the X-direction: amplitude (scaled to maximum value, left) and phase (right) of the surface normal displacement for (a) $X + 0^{\circ}$, (b) $X + 45^{\circ}$, (c) $X + 52.8^{\circ}$, (d) $X + 90^{\circ}$. Propagation direction is parallel to x and from left to right, IDTs are located at $x = 0$ with 2 mm aperture centered at $y = 0$. Frequencies are chosen according to $|S_{11}|_{min}$ (Table 2, f_{exp}).

travelling characteristics arise. Fig. 11 shows the resultant wave field for all four propagation directions. The typical pattern of 1DsSAW, possessing periodical changes of minimum and maximum amplitude in propagation direction, can be observed regardless of the particular propagation angle. The minimum amplitude is close or equal to zero indicating a nearly pure standing wave. The distance between two sequent minima/maxima is approximately 75 µm which corresponds to half of the SAW wavelength. In case of $\theta = 0^{\circ}$, $\theta = 52.8^{\circ}$ and $\theta = 90^{\circ}$ almost ideal symmetry with respect to $y = 0$ (perpendicular to the propagation direction) can by observed for amplitude. The presence of beam steering for $\theta = 45^{\circ}$ causes an asymmetry comparable to that of tSAW pattern depicted in Fig. 7: both counter-propagating SAWs exhibit negative power flow angle because the IDTs are rotated by $\theta = +45^{\circ}$.

Beam steering also causes a pattern of the standing wave which is less pronounced compared to the other orientations, i.e. amplitude

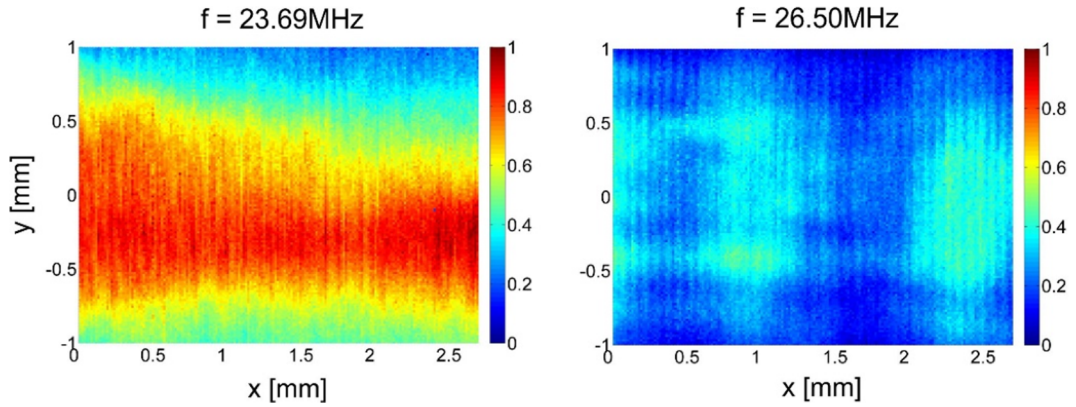

Fig. 8. Comparison of surface normal wave field amplitude in front of IDT oriented at $X + 45^{\circ}$ for f_{exp} = 23.69 MHz and 26.50 MHz. Amplitude is scaled to maximum value at 23.69 MHz.

minima and maxima are considerably less distinguished. For a pure standing wave (infinite standing wave ratio) the phase exhibits abrupt changes of ± 180° in propagation direction with a periodicity of half of the SAW wavelength. 1DsSAW for $X + 0^{\circ}$ (Fig. 11a) almost shows an ideal phase pattern of a pure standing wave with a phase shift of 180°. Abrupt phase changes in propagation direction also can be observed for and $X + 52.8^{\circ}$ and $X + 90^{\circ}$ (Fig. 11c and d), even though the phase shift partially is below 180°. Additionally, continuous phase changes perpendicular to the propagation direction occur indicating relevant travelling wave portions within the 1DsSAW. These are caused by angular SAW components as well as by slight misalignment of angular substrate orientation. The phase pattern of 1DsSAW for $X + 45^{\circ}$ (Fig. 11b) features continuous changes in propagation direction that become more pronounced for $|y| > 0$. Thus, the impact of travelling wave components on the standing wave field (1DsSAW) becomes maximum for $X + 45^{\circ}$ due to beam steering. In general, the higher the portion of travelling wave components, the lower the standing wave ratio converging to one for pure travelling waves.

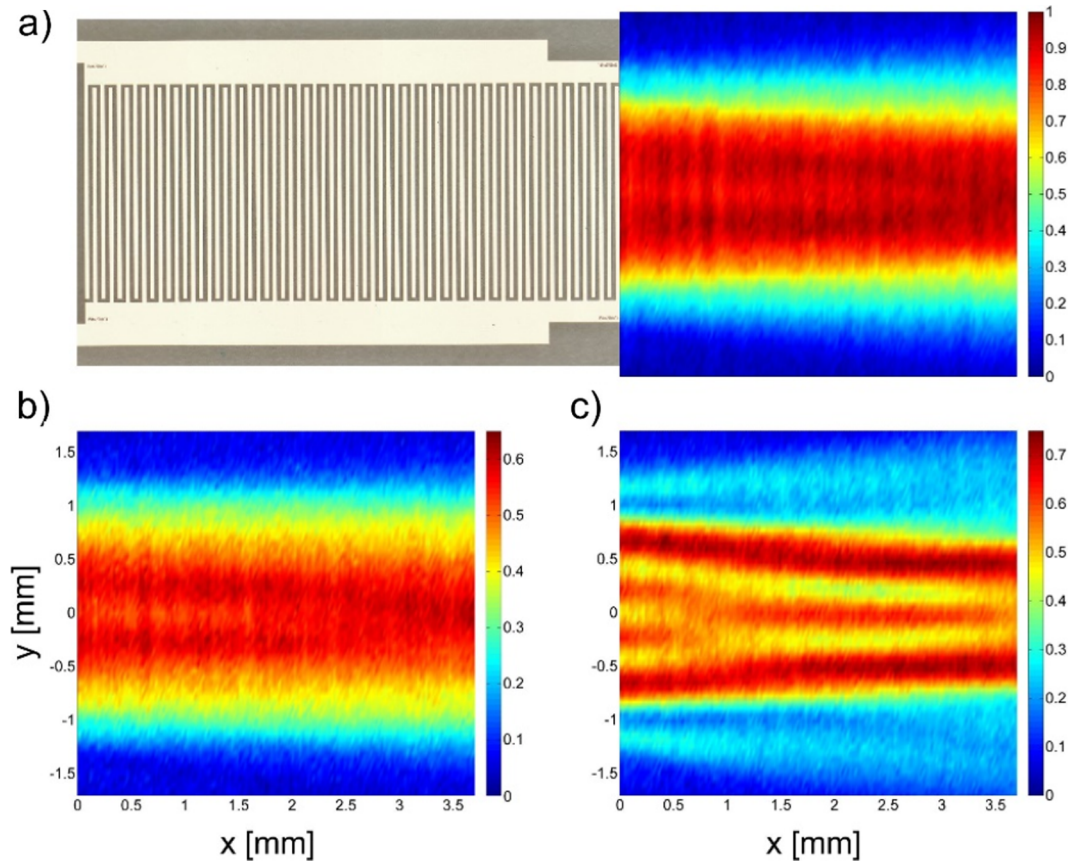

Fig. 9. Frequency dependence of tSAW wave field in front of IDT orientated at $X + 0^{\circ}$: (a) f = 25.55 MHz, (b) f = 25.40 MHz and (c) f = 26.45 MHz (amplitudes are scaled to maximum value at 25.55 MHz).

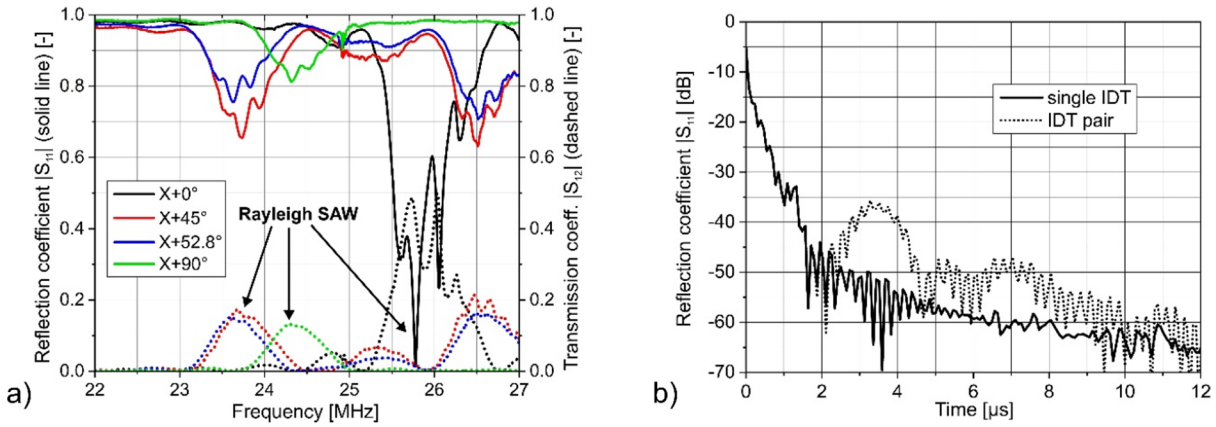

Fig. 10. Electrical characterization of IDT pairs differently oriented w.r.t. X-direction: (a) reflection ($|S_{11}|$) and transmission ($|S_{12}|$) coefficients, (b) time domain reflection coefficients ($|S_{11}|$) for single IDT and IDT pair at $X + 0^{\circ}$.

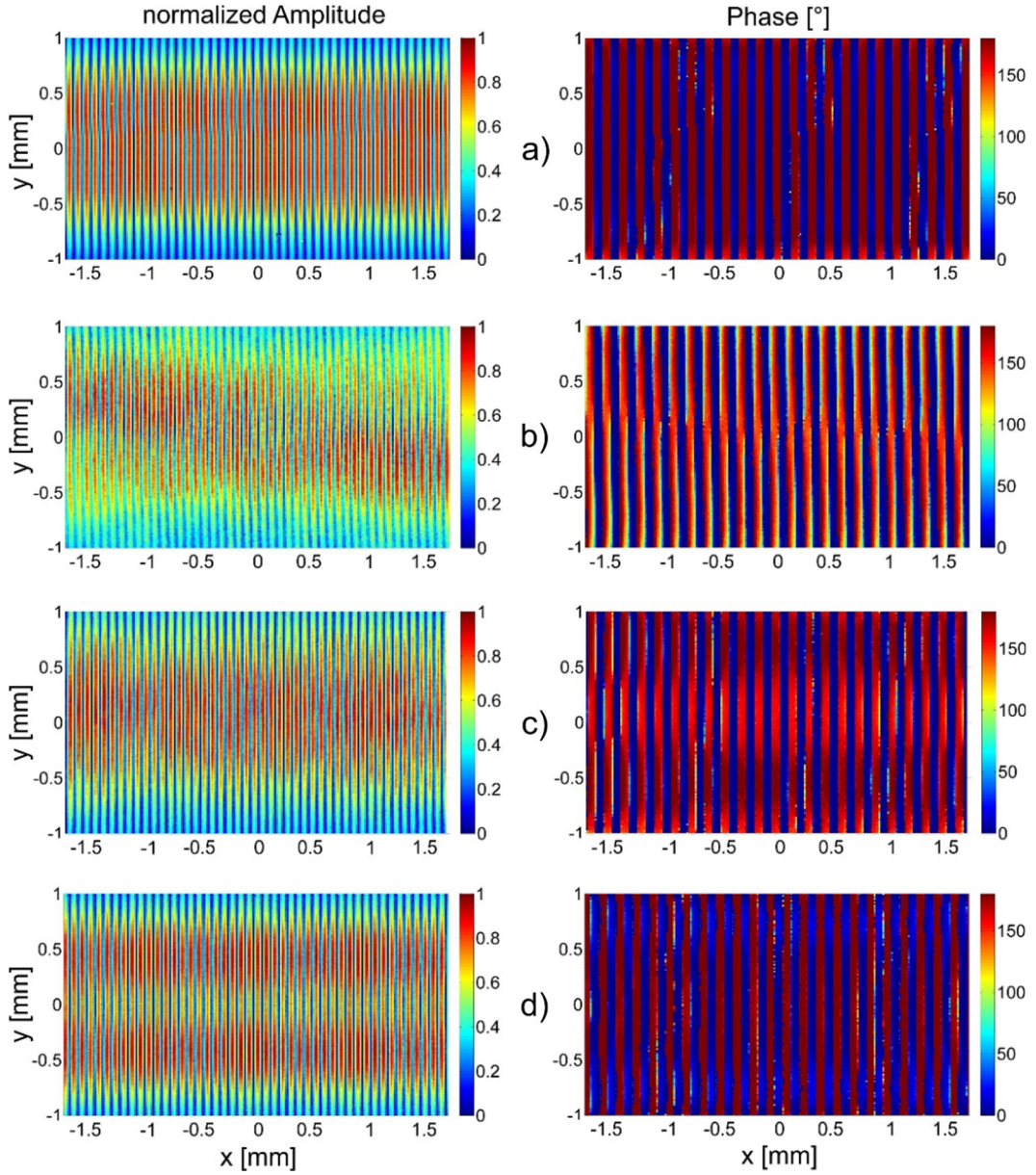

Fig. 11. Wave fields between IDT pairs with different orientation w.r.t. to X-axis: amplitude (scaled to maximum value, left) and phase (right) of surface normal displacement for (a) $X + 0^{\circ}$, (b) $X + 45^{\circ}$, (c) $X + 52.8^{\circ}$, (d) $X + 90^{\circ}$. Propagation direction is parallel to x, IDTs are located at $x = -1.75$ mm and $x = 1.75$ mm with the aperture center at $y = 0$. Frequencies are chosen according to $|S_{11}|_{min}$ (Table 2, f_{exp}).

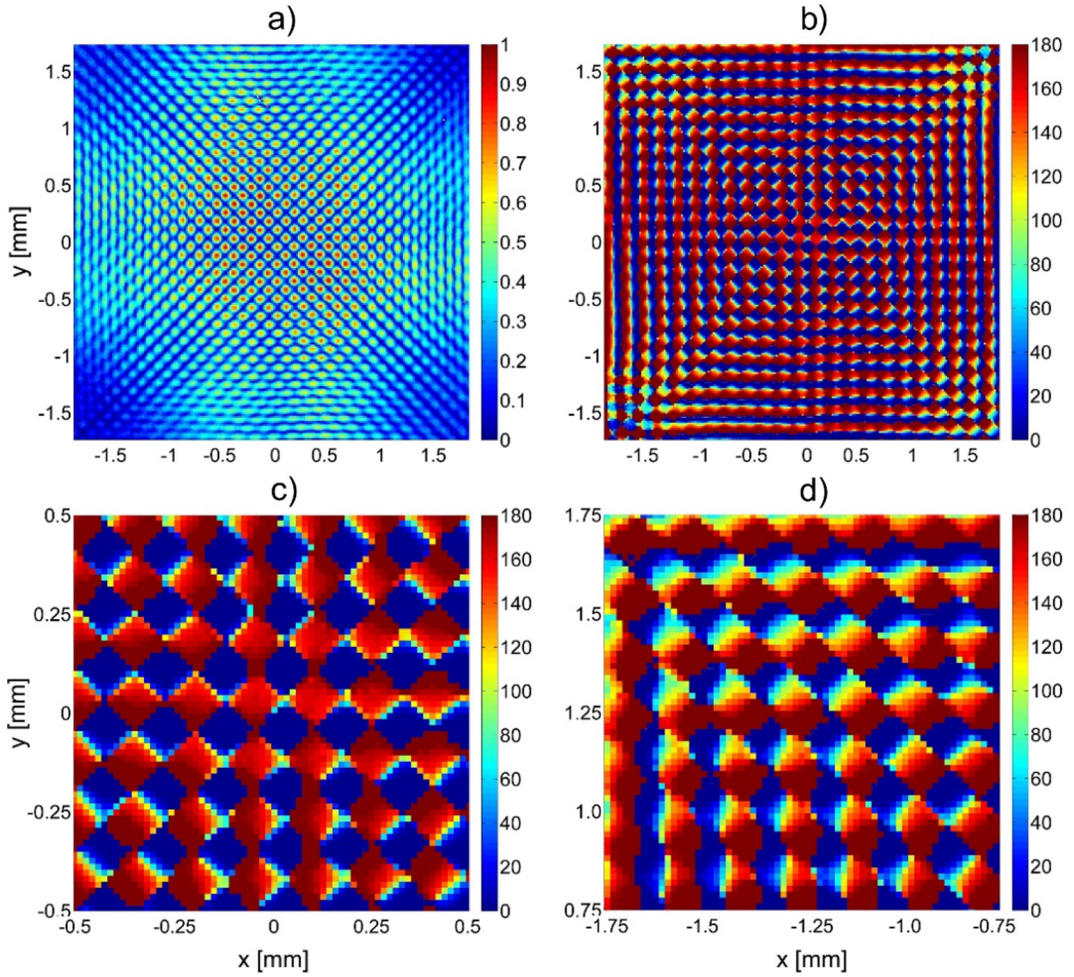

Fig. 12. Wave field between two orthogonal aligned IDT pairs (orientation: $X \pm 45^{\circ}$): (a) amplitude (scaled to maximum value) and (b) phase (in degree) of surface normal displacement at $f_{exp} = 23.69$ MHz. Detailed views of phase pattern are given for the center region (c) and the left upper region (d). Propagation directions are parallel to x and y. IDTs are located at $x, y = -1.75$ mm and $x, y = 1.75$ mm with the aperture center at $y, x = 0$.

4.3. Standing SAW in two dimensions (2DsSAW)

If all four IDTs within one setup (cf. Fig. 4) are used to excite SAWs, two one-dimensional standing SAWs (1DsSAW) will superimpose evoking a more complex wave field within two propagation directions. In case of $X \pm 45^{\circ}$ and $X \pm 52.8^{\circ}$ both IDT pairs possess the same electro-acoustic behavior, based on the same SAW coupling coefficient and velocity. Fig. 12 illustrates the resulting wave field for $X \pm 45^{\circ}$. The displacement amplitude shows a complex pattern of minima and maxima arising from the superposition of both 1DsSAWs. Overall minima appear in straight lines arranged at ± 45° with respect to the primary propagation directions of both 1DsSAWs that rather can be seen from the phase of surface normal displacement indicating an almost perpendicular orientation of both 1DsSAWs to each other (Fig. 12b). However, the slightly twisted phase pattern depicts the presence and influence of beam steering and travelling SAW which also can be seen in the phase pattern of 1DsSAW (Fig. 11). While the very center of the wave field is dominated by discontinuous phase changes indicating standing SAW (Fig. 12c), the presence of travelling SAW components increases with distance from the center to the corners of the wave field (Fig. 12d). The influence of excitation frequency on the 2DsSAW wave field is exemplary shown in supplemental video 2 for $X \pm 45^{\circ}$.

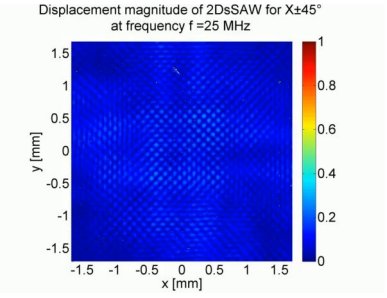

video 2.

Fig. 13 illustrates the resulting wave field for $X \pm 52.8^{\circ}$. Here, one propagation direction is parallel to the x-coordinate and the second one is parallel to $x + 74.4^{\circ}$. The propagation directions can also be seen from the phase fronts indicating the non-orthogonal IDT orientation. The amplitude again shows a complex pattern of minima and maxima arising from the superposition of both 1DsSAWs. The phase pattern is dominated by discontinuous phase changes of standing SAW, but due to the non-orthogonal IDT arrangements and, thus, the non-orthosymmetric amplitude distribution, also regions with continuous phase changes exist, indicating the presence of travelling wave components.

In the setup with two IDT pairs, aligned at $X + 0^{\circ}$ and $X + 90^{\circ}$,

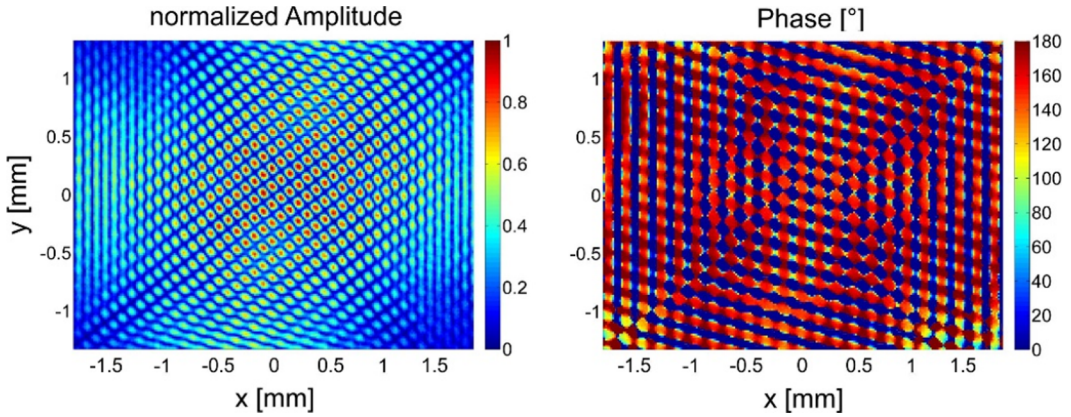

Fig. 13. Wave field between two IDT pairs (orientation: $X \pm 52.8^{\circ}$): amplitude (scaled to maximum value) and phase of surface normal displacement at f_{exp} = 23.64 MHz. Propagation directions are parallel to x and $x + 74.4^{\circ}$, corresponding IDTs are located at a distance of 1.75 mm to the center line of aperture at y, $x = 0$.

respectively, different SAW propagation properties exist. The difference of phase velocities yields different resonance frequencies due to equal periodicity of all IDTs (Table 1). If both IDT pairs are excited at their own resonance frequency, a standing wave within two dimensions cannot be achieved because the resultant frequency difference

$$\Delta f = 25.75\ \text{MHz} - 24.3\ \text{MHz} = 1.45\ \text{MHz}$$

between both directions causes a corresponding period $T_{beat} = 1/\Delta f \approx$

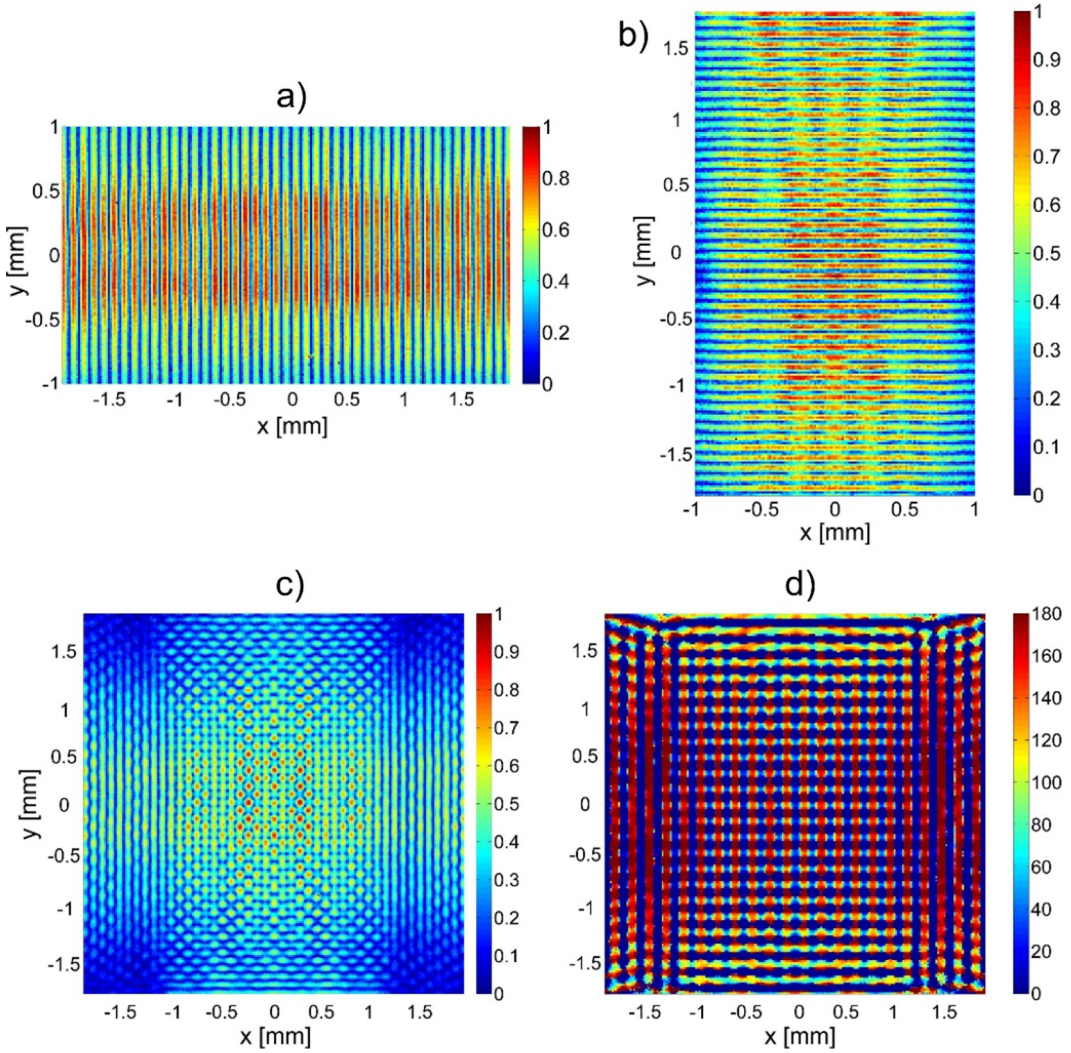

Fig. 14. Wave fields between two IDT pairs (orientation: $X + 0^{\circ}$ and $X + 90^{\circ}$) at 25.35 MHz: (a, b) surface normal displacement amplitude (scaled to maximum value) of 1DsSAWs for both individual propagation directions as well as (c) amplitude (scaled to maximum value) and (d) phase (in degree) of 2DsSAW. Propagation directions are parallel to x ($X + 0^{\circ}$) and y ($X + 90^{\circ}$). IDTs are aligned at the edges of the measured wave fields.

0.69 µs which is approximately 17 times the period of the SAW. Thus, an additional time-variant component appears within the wave field (see supplemental video 3) and it cannot be represented by static diagrams anymore. In principle, a common, intermediate frequency can be chosen, which allows the excitation of a 2DsSAW with the same frequency but slightly different wavelengths of both 1DsSAWs. For f= 25.35 MHz, the corresponding wave fields of both 1DsSAWs as well as of the 2DsSAW can be seen in Fig. 14. Beside the poor electro-acoustic efficiency of all IDTs at the intermediate frequency (cf. Fig. 10), a noticeable excitation of SAW can be observed for both directions. However, generating a 2DsSAW this way is not relevant for practical purposes and it would be more appropriate to design IDTs with different wavelengths in order to achieve the same operation frequency, if $X + 0^{\circ}$ and $X + 90^{\circ}$ propagation direction should be used on 128°Y $LiNbO_3$. In this case, the distance between minima/maxima would be slightly different for the $X + 0^{\circ}$ and $X + 90^{\circ}$ direction.

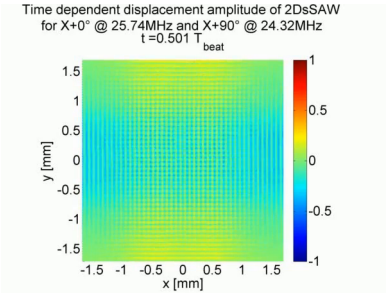

video 3.

5. Conclusions

Different arrangements of interdigital transducers on 128° rotated Y-cut $LiNbO_3$ substrate, capable of the generation of travelling and standing surface acoustic wave fields, were investigated within this work. SAW propagation directions were selected based on fundamental effects of wave propagation (phase velocity, beam steering, coupling coefficient) on the anisotropic substrate commonly used for microfluidic actuators. The different IDT arrangements presented within this work can be regarded as the most basic setups since all other layouts result in a mixture of the effects mentioned here.

For microfluidic applications including fluid mixing (tSAW) and particle sorting (1DsSAW) necessitating one SAW propagation direction, the X-propagation direction ($X + 0^{\circ}$) typically is the best choice since it provides the highest coupling coefficient, i.e. the most efficient SAW excitation together with no beam steering. In principle, the $X + 90^{\circ}$ direction also can used for these purposes but will show a lower coupling coefficient. Both directions are capable to generate well shaped beam profiles (tSAW) as well as to produce almost pure standing waves for 1DsSAW. Note, that both features are very sensitive to the exact excitation frequency and require stable and well-defined electrical excitation signals. In case of acoustic tweezers based on 2DsSAW, two different propagation directions need to be combined and at least one direction needs to be different from the X-direction. The combination of $X + 0^{\circ}$ and $X + 90^{\circ}$ is the most complicated layout as it involves different phase velocities resulting in different frequencies for equal wavelength or different wavelengths for equal frequency in both directions. Besides, the according coupling coefficients are different and need to be compensated by IDT design or different driving power levels. In principle, making use of other propagation directions, e.g. $X \pm 45^{\circ}$ or $X \pm 52.8^{\circ}$, can overcome these drawbacks. However, additional effects such as beam steering (for $X \pm 45^{\circ}$) and non-orthogonality (for $X \pm 52.8^{\circ}$) have also to be considered. Besides the propagation directions used to excite the SAW, the intended SAW field also depends on the specific arrangement of the IDTs, i.e. the distance between two opposing IDTs due to e.g. SAW diffraction, as well as on the geometric parameters of the IDTs, i.e. the period, the length and the aperture of the transducers. All parameters of the SAW device layout, including anisotropic substrate characteristics, need to be chosen with respect to the intended features of the SAW field. The lateral distribution of both, the amplitude and the phase of displacement essentially affects the microfluidic actuation capabilities.

Electrical S-parameter characterization provides sufficient and easy-to-gather information for choosing the proper frequency for efficient operation of the interdigital transducer regardless of the propagation direction. Nevertheless, measurement of the surface acoustic wave field gives additional, sometimes even indispensable information for a proper design of SAW-driven microfluidic devices, particularly with regard to the positioning and dimensioning of microfluidic vessels. Even for simple microfluidic setups containing only a single IDT for the excitation of a travelling SAW that encounters a microchannel for the purpose of fluid mixing, detailed knowledge of the SAW beam profile inside the channel is mandatory for a fundamental understanding of acoustic streaming [28,32]. In case of a standing SAW within one lateral dimension (1DsSAW) used for, e.g. the atomization of fluids, wave field characterization gives a hint at which position between both IDTs the maximum displacement amplitude, and thus most effective droplet production will appear [16,17]. Acoustic tweezers typically driven by 2DsSAW, rely on precisely tailored SAW wave fields in order to ensure bulk wave nodes in the fluid to be at defined position and to be stationary. The latter request necessitates the presence of pure standing SAW patterns. For IDT arrangements exhibiting beam steering, resulting wave fields possess relevant travelling wave portions that can cause acoustically induced fluid streaming disturbing distinctive fluid zones with no lateral streaming ('tweezing spots') and thus, reduce performance of acoustic tweezers.

Investigations within this work are focused on fundamental effects of SAW superposition on planar substrates. Future investigations need to consider the presence of microfluidic vessel and fluid, too. For though, the detailed knowledge of standing SAW fields is not the answer to all questions for microfluidic applications, but a very important starting point for simulations and for the understanding of the generated bulk acoustic wave fields inside the fluid as well as for particle and cell manipulation.

Declaration of Competing Interest

The authors declare that they have no known competing financial interests or personal relationships that could have appeared to influence the work reported in this paper.

Acknowledgements

This work was supported by DFG under grant SCHM 2365/16-1. The authors would like to thank the members of the IFW cleanroom for device production and the members of the IFW workshop for production of chip holder.

References

[1] X. Ding, et al., Surface acoustic wave microfluidics, Lab. Chip. 13 (2013) 3626.
[2] J.K. Luo, Y.Q. Fu, W.I. Milne, Acoustic Wave Based Microfluidics and Lab-on-a-Chip, in: M.G. Beghi (Ed.), Modeling and Measurement Methods for Acoustic Waves and for Acoustic Microdevices, Intech Open, 2013, pp. 515–556.
[3] L.Y. Yeo, J.R. Friend, Surface Acoustic Wave Microfluidics, Ann. Rev. Fluid Mech. 46 (2014) 379.
[4] W. Connacher, et al., Micro/nano acoustofluidics: materials, phenomena, design, devices, and applications, Lab. Chip. 18 (2018) 1952.
[5] A. Renaudin, et al., SAW nanopump for handling droplets in view of biological applications, Sens. Actuators B Chem. 113 (2006) 389.
[6] C.D. Wood, et al., Formation and manipulation of two-dimensional arrays of micron-scale particles in microfluidic systems by surface acoustic waves, Appl. Phys. Lett. 94 (2009) 054101.
[7] M. Sesen, T. Alan, A. Neild, Microfluidic on-demand droplet merging using surface acoustic waves, Lab. Chip. 14 (2014) 3325.

[8] L.Y. Yeo, J.R. Friend, Ultrafast microfluidics using surface acoustic waves, Biomicrofluidics 3 (2009) 1.
[9] K.M. Seemann, J. Ebbecke, A. Wixforth, Alignment of carbon nanotubes on pre-structured silicon by surface acoustic waves, Nanotechnology 17 (2006) 4529.
[10] Y. Chen, et al., Continuous enrichment of low-abundance cell samples using standing surface acoustic waves (SSAW), Lab. Chip. 14 (2014) 924.
[11] Y. Ai, C.K. Sanders, B.L. Marrone, Separation of escherichia coli bacteria from peripheral blood mononuclear cells using standing surface acoustic waves, Anal. Chem. 85 (2013) 9126.
[12] L. Meng, et al., Transportation of single cell and microbubbles by phase-shift introduced to standing leaky surface acoustic waves, Biomicrofluidics 5 (2011) 044104.
[13] J. Nam, et al., Density-dependent separation of encapsulated cells in a microfluidic channel by using a standing surface acoustic wave, Biomicrofluidics 6 (2012) 024120.
[14] X.J. Hu, et al., Precise label-free leukocyte subpopulation separation using hybrid acoustic-optical chip, Lab. Chip. 18 (2018) 9.
[15] D.J. Collins, et al., Acoustic tweezers via sub–time-of-flight regime surface acoustic waves, Sci. Adv. 2 (2016) e1600089.
[16] A. Winkler, et al., SAW-based fluid atomization using mass-producible chip devices, Lab. Chip. 15 (2015) 3793.
[17] A. Winkler, et al., Compact SAW aerosol generator, Biomed. Microdevices 19 (2017) 9.
[18] X.Y. Ding, et al., On-chip manipulation of single microparticles, cells, and organisms using surface acoustic waves, PNAS 109 (2012) 11105.
[19] L. Meng, et al., On-chip targeted single cell sonoporation with microbubble destruction excited by surface acoustic waves, Appl. Phys. Lett. 104 (2014) 073701.
[20] T.D. Nguyen, et al., Patterning and manipulating microparticles into a three-dimensional matrix using standing surface acoustic waves, Appl. Phys. Lett. 112 (2018) 213507.
[21] F. Guo, et al., Three-dimensional manipulation of single cells using surface acoustic waves, PNAS 113 (2016) 6.
[22] D.J. Collins, et al., Two-dimensional single-cell patterning with one cell per well driven by surface acoustic waves, Nat. Comm. 6 (2015) 8686.
[23] M.S. Brugger, et al., Orchestrating cells on a chip: Employing surface acoustic waves towards the formation of neural networks, Phys. Rev. E 98 (2018) 6.
[24] D. Morgan, Surface Acoustic Wave Filters, Academic Press, Oxford, 2007.
[25] A.N. Darinskii, M. Weihnacht, H. Schmidt, Acoustomicrofluidic application of quasi-shear surface waves, Ultrasonics 78 (2017) 10.
[26] G. Kovacs, et al., Improved material constants for LiNbO3 and LiTaO3, in: 1990 IEEE Symposium on Ultrasonics. Honolulu, HI, USA, 1990. https://doi.org/10.1109/ULTSYM.1990.171403.
[27] C. Devendran, et al., Huygens-fresnel acoustic interference and the development of robust time-averaged patterns from traveling surface acoustic waves, Phys. Rev. Lett. 118 (2017) 154501.
[28] A. Fakhfouri, et al., Surface acoustic wave diffraction driven mechanisms in microfluidic systems, Lab. Chip. 18 (2018) 2214.
[29] A. Winkler, et al., Towards efficient surface acoustic wave (SAW)-based microfluidic actuators, Sen. Actuators A Phys. 247 (2016) 259.
[30] A. Winkler, S.B. Menzel, H. Schmidt, SAW-grade SiO2 for advanced microfluidic devices, in: Smart Sensors, Actuators, and MEMS IV. Dresden, Germay, 2009.
[31] R. Weser, A. Sotnikov, H. Schmidt, Advanced characterization of surface acoustic wave fields at high temperature, in: 2018 IEEE International Ultrasonics Symposium (IUS). Kobe, Japan, 2018. https://doi.org/10.1109/ULTSYM.2018.8579907.
[32] F. Kiebert, et al., 3D measurement and simulation of surface acoustic wave driven fluid motion: a comparison, Lab. Chip. 17 (2017) 2104.